Global conditions in the solar corona from 2010 to 2017

Morgan, Huw; Taroyan, Youra

Published in:
Science Advances

DOI:
10.1126/sciadv.1602056

Publication date:
2017

Citation for published version (APA):
Morgan, H., & Taroyan, Y. (2017). Global conditions in the solar corona from 2010 to 2017. *Science Advances*, *3*(7), 1-13. [e1602056]. https://doi.org/10.1126/sciadv.1602056

ASTROPHYSICS

Global conditions in the solar corona from 2010 to 2017

Huw Morgan* and Youra Taroyan

Through reduction of a huge data set spanning 2010–2017, we compare mean global changes in temperature, emission measure (EM), and underlying photospheric magnetic field of the solar corona over most of the last activity cycle. The quiet coronal mean temperature rises from 1.4 to 1.8 MK, whereas EM increases by almost a factor of 50% from solar minimum to maximum. An increased high-temperature component near 3 MK at solar maximum drives the increase in quiet coronal mean temperature, whereas the bulk of the plasma remains near 1.6 MK throughout the cycle. The mean, spatially smoothed magnitude of the quiet Sun magnetic field rises from 1.6 G in 2011 to peak at 2.0 G in 2015. Active region conditions are highly variable, but their mean remains approximately constant over the cycle, although there is a consistent decrease in active region high-temperature emission (near 3 MK) between the peak of solar maximum and present. Active region mean temperature, EM, and magnetic field magnitude are highly correlated. Correlation between sunspot/active region area and quiet coronal conditions shows the important influence of decaying sunspots in driving global changes, although we find no appreciable delay between changes in active region area and quiet Sun magnetic field strength. The hot coronal contribution to extreme ultraviolet (EUV) irradiance is dominated by the quiet corona throughout most of the cycle, whereas the high variability is driven by active regions. Solar EUV irradiance cannot be predicted accurately by sunspot index alone, highlighting the need for continued measurements.

INTRODUCTION

Studies of the corona are usually limited to studies of particular regions or to small statistical studies [for example, the work of Fisher *et al.* (*1*)]. This work presents an initial summary of results gained from a differential emission measurement (DEM) analysis of a large set of extreme ultraviolet (EUV) observations made over several years. From these results, the mean global coronal temperature and total emission measure (EM; similar to column mass) are estimated over several years and are compared to measurements of the photospheric magnetic field. To our knowledge, this is the first report of its kind that presents global long-term values of coronal conditions over most of a solar activity cycle. This paper is an overview of the main results, with a detailed analysis reserved for future studies.

The solar corona is composed of both closed magnetic loops emerging from the photosphere and "open" magnetic field regions that form the heliosphere. Closed-field active regions are hot (>~2 MK) (*2*–*4*), open-field regions are colder (<~1.1 MK) (*5*–*8*), and in between is the quiet corona (~1.5 MK) (*9*, *10*). Models for coronal heating fall in two main categories: ac mechanisms that convert magnetic waves to plasma thermal energy (*11*–*14*), and dc mechanisms based on small-scale magnetic reconnection events (*15*–*17*). There are several outstanding observational challenges: the lack of direct measurements of the coronal magnetic field, the line-of-sight (LOS) problem (observations of the optically thin corona have contributions from an extended LOS), and the difficulty of observing small-scale waves or reconnection events, given limited spatial and temporal resolution. There are several observational and theoretical reasons to support the bulk heating of plasma in the chromosphere, some proportion of which subsequently flows into the corona at a rate that maintains a high temperature, although the debate has not been settled (*18*–*20*). Regardless of where the bulk heating occurs, measurements of coronal characteristics are important to understand the heating processes. This paper aims to present a solar-cycle overview of global changes in DEM in quiet corona and active regions. For this global overview, we averaged values over broad swathes of the corona: for example, we do not consider here any latitudinal dependence of various regions. Furthermore, we do not attempt here to track individual regions over time, and instead, we concentrate on global values gained from a synoptic, meridional scan of the corona. A more detailed study is reserved for future works that will more directly link our results to the coronal energy budget and heating models, as well as tracking changes in individual regions over long time scales.

Although the total solar irradiance at Earth varies very little, the relative variance in the EUV is as large as the mean irradiance (*21*). This EUV light interacts with Earth's thermosphere and stratosphere and may affect climate in a "top-down" process in regions such as northern Europe (*22*). One uncertainty is the lack of historical solar EUV measurements. In contrast, sunspot records, probably the most recognized index of solar activity, go centuries back. Studies of solar effect on climate must make use of such long-term proxies for the solar irradiance variation (*23*). Our analysis of global coronal conditions gives an estimate of the relative contributions of the quiet corona and active regions to EUV irradiance—a key step in an estimate of EUV irradiance based simply on active region area or sunspot number. We present here an initial summary of our estimate of the coronal EUV irradiance gained from the global DEM analysis. Future work will use the results in more detail and, in particular, will seek a more comprehensive link between total EUV irradiance, the solar cycle, and the proportion of the solar corona defined as quiet corona or active regions, as well as the size, latitude, and age of active regions. This overview does not investigate the EUV irradiance from individual active regions and does not consider the irradiance from temperature ranges beyond those given by the DEM curves obtained from the particular EUV observations; thus, the chromosphere and transition region irradiance is excluded.

Since mid-2010, the EUV emission of the solar corona is imaged in high spatial and temporal resolution by the multiple channels of the Atmospheric Imaging Assembly [AIA (*24*)] aboard the Earth-orbiting Solar Dynamics Observatory (SDO) (see Fig. 1). Each channel is dominated by emission from highly ionized elements; thus, the measurement is related to the coronal density and temperature. Another instrument aboard SDO, the Helioseismic and Magnetic Imager [HMI (*25*)], uses Zeeman splitting to measure the photospheric magnetic field in high

Physics Department, Aberystwyth University, Aberystwyth, Ceredigion SY23 3BZ, UK.
*Corresponding author. Email: hmorgan@aber.ac.uk

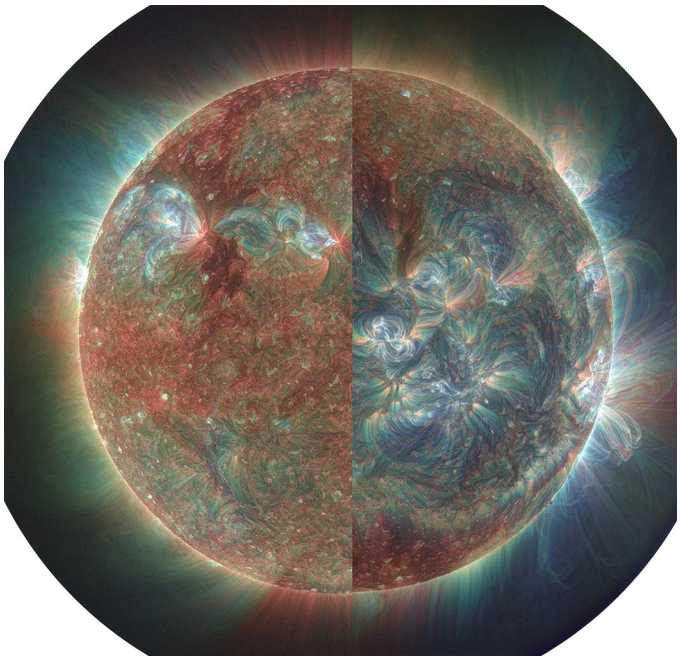

Fig. 1. The changing appearance of the corona from solar minimum to maximum. These images are taken by AIA/SDO in EUV toward the end of the latest solar minimum activity period in May 2010 (left half) and during the current solar maximum period in December 2014 (right half). The three-color red-green-blue image channels are composed of observations made in three AIA channels: 171, 193, and 211 Å, respectively, corresponding to their most dominant emission lines of Fe IX, Fe XII, and Fe XIV with formation temperatures of ~0.7, 1.2, and 2.0 MK. The image has been processed using multiscale Gaussian normalization (*64*).

resolution. A third instrument, the EUV Variability Experiment [EVE (*26*)], measures the disk-integrated EUV spectrum in high spectral resolution.

RESULTS

Figure 2 shows synoptic maps of coronal temperature, EM, and photospheric magnetic field during March to April 2011. The maps of Fig. 2 clearly show the three general large-scale regions of the corona. Coronal holes are cooler, low-mass regions usually situated at the poles, particularly during solar minimum. Active regions are hot, high-mass regions of enhanced magnetic field, distributed within ±45° of the equator, associated with sunspots and with a typical life span of a few solar rotations (months). The broad regions outside of coronal holes and active regions, covering most of the solar disk, are quiet Sun/corona. The magnetic field magnitude in the quiet Sun, when smoothed over small spatial regions, is far weaker than that of active regions, on the order of a few Gauss. This study focuses on global changes to the mean field over long time periods. Without smoothing, the field is highly variable down to small spatial scales and can contain small regions of high field concentrations. Because we are interested primarily here in the coronal field, median smoothing is applied on the signed photospheric radial magnetic field; thus, most of the small-scale concentrations of intense field present even in the quiet Sun are reduced. Further spatial smoothing is then applied to the field magnitude (see Methods). Active regions and quiet coronal regions are identified and segmented (as shown in Fig. 2 and described in Methods), enabling separate analysis of their time series. These global time series show large short-term variations over periods of a solar rotation. Considerable smoothing over time is applied to reduce the dominant solar rotation modulation and to reveal longer-term global trends, also described in Methods.

For a simple representation of mean global trends, this study uses a mean temperature weighted by the EM, detailed further in Methods. For each pixel, we used measurements in several wavelength channels to estimate a DEM (or emission as a function of temperature) (*27*). DEM curves can be highly peaked at a single temperature, particularly for quiet coronal regions —the weighted mean temperature is therefore a meaningful representation of the dominant emitting plasma temperature. Active regions show very broad DEM peaks; therefore, only the variations in the mean temperature over time, or between regions, are meaningful, in relation to the changes in the underlying DEM profile. For global values of EM, we integrated the DEM profiles over the considered temperature range. A future study will provide a more detailed analysis of changes in DEM profiles over time.

Figure 3A shows global quiet corona properties from 2010 to 2017. EM and magnetic field are highly correlated and show a rapid rise following solar minimum in 2010. They maintain high values throughout solar maximum, before declining rapidly from 2015 to present. Temperature is less correlated over short time scales and shows a more gradual rise from minimum to maximum in 2014 and 2015 and a shallower decline from 2015 to present. Figure 4A shows that the quiet corona is dominated by emission from plasma at ~1.6 MK—this is the most probable temperature and remains approximately constant over the solar cycle. The rise and decline in mean temperature are most strongly influenced by the strength of a secondary peak in emission at ~3 MK, which is most apparent between mid-2012 and 2015. The solar cycle thus modulates a secondary peak in the quiet coronal DEM near 3 MK, weak at solar minimum, and peaking between mid-2012 and 2015. Similar bimodal quiet Sun temperature distributions have been found during solar minimum in 2010, with a main DEM peak at 1.47 MK and a hotter secondary peak at 2.57 MK, which is in agreement with this study (*28*). The hot secondary emission may be associated with regions of active region decay or increased small-scale bipole emergence: for example, a recent study has shown that such bipoles have a peak DEM at ~2 MK, whereas their DEM-weighted mean temperature is closer to the mean quiet Sun at ~1.6 MK (*29*). A study of quiet Sun regions using the EUV Imaging Spectrometer (EIS; part of the Hinode mission) during 2007 suggests that the quiet Sun has a "universal" DEM profile up to ~1.6 MK, scaled only by the absolute value of emission (*30*). Figure 4A shows that the DEM profile below 1.6 MK varies over the solar cycle; thus, the concept of a universal quiet Sun DEM may only be valid over short time scales or for selected regions. Furthermore, the EIS study was limited to emission lines that are sensitive to below ~2.5 MK, and thus, the hot secondary peak near 3 MK was not considered.

The mean active region temperature, EM, and magnetic field over the 2010–2017 period are plotted in Fig. 3B. There is very high correlation between properties (>60% between EM and magnetic field and >75% between EM and temperature). Large variations in magnetic field, EM, and temperature occur on time scales of months, superimposed on a small overall increase and decrease with the solar cycle. Figure 4B shows that active region DEMs are peaked at a temperature somewhat higher than that of the quiet corona and that the peak is very broad, with emission extending to high temperatures. These profiles, which are averaged over all active regions present in a given time bin, show general agreement with previously published DEM profiles integrated over whole active regions (*4*, *31*, *32*). The predominant active region temperature is around 1.8 MK, with hot cores at a temperature closer to

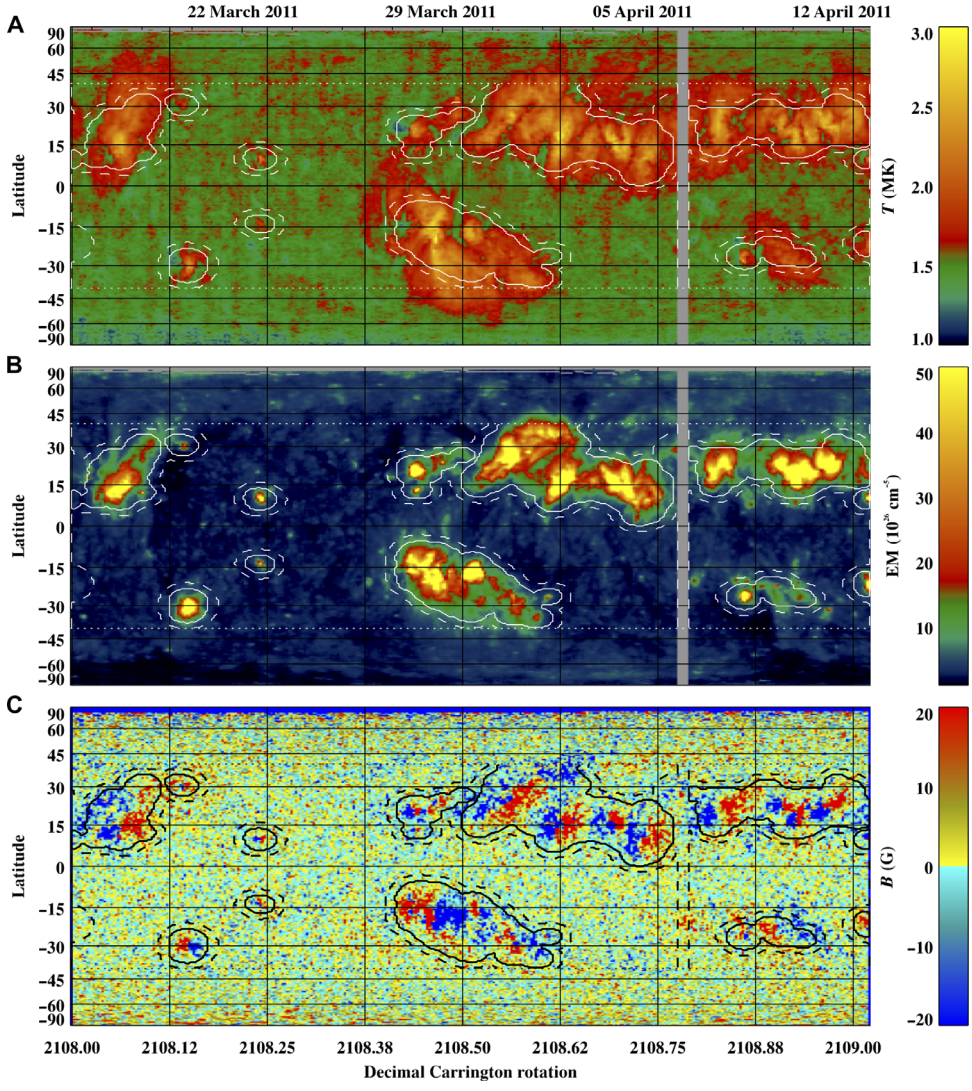

Fig. 2. Synoptic maps showing the varying properties of the corona and photosphere over a whole solar rotation. Shown here are (**A**) mean temperature, (**B**) EM, and (**C**) radial magnetic field component for a whole solar rotation during 04 March 2011. The *y* axis shows latitude on the solar disk, on a sine latitude scaling. The two horizontal dotted lines indicate the latitudinal range within ±40° of the equator (areas outside are not included for further study). Areas defined as active regions are shown within unbroken contours. Areas outside the dashed contours are considered as quiet corona. See Methods for more details on the identification of regions.

3 MK. Similar to the quiet corona, the maximum DEM peak at ~1.8 MK remains fairly constant over the solar cycle, and variations in mean temperature are caused by variations in the emission at higher temperatures. The only consistent long-term trend is a decrease in high-temperature emission after mid-2014, leading to a gradual decrease in the mean temperature to present. Figure 3B shows that global, solar cycle variations caused by active regions (such as EUV irradiance measures) are driven primarily by the change in active region area, closely related to sunspot area, and not by a cyclic change in active region conditions. That is, despite large variation in properties from one active region to the other, and over time scales of months, there is no strong solar cycle effect in mean active region properties except for the interesting decrease in high-temperature emission from mid-2014 to present. An active region during solar maximum is not more likely to be hotter, or to be emitting more in the EUV, than an active region at any other time in the solar cycle. This has implications for long-term models of solar activity (*33*), where the mean characteristics of emerging active regions should remain approximately constant over the cycle. We emphasize that there is very large variation in mean properties from one active region to the next: Considerable convolution over time is used to gain the smooth results shown in Figs. 3B and 4B.

As expected, active region area and smoothed daily sunspot area show great similarity (*34*), as shown in Fig. 3C. Both show multiple peaks, with sunspot area showing localized peaks a month or two earlier than peaks in the active region area. The cross-correlation between the two values is high at 62% at a lag of 45 days. The lag is a large-scale effect related to the general growth of large active region complexes above sunspot groups and not to the growth of individual active regions above individual sunspots. As sunspot numbers increase, and longitudinally extended bands of sunspots appear during the rise to solar maximum, the individual, smaller, active regions associated with individual sunspots (or sunspot pairs) form connecting complexes of large loops and, if the groupings are dense enough, will form large active region complexes. Larger active regions are more likely to form during solar maximum (*35*).

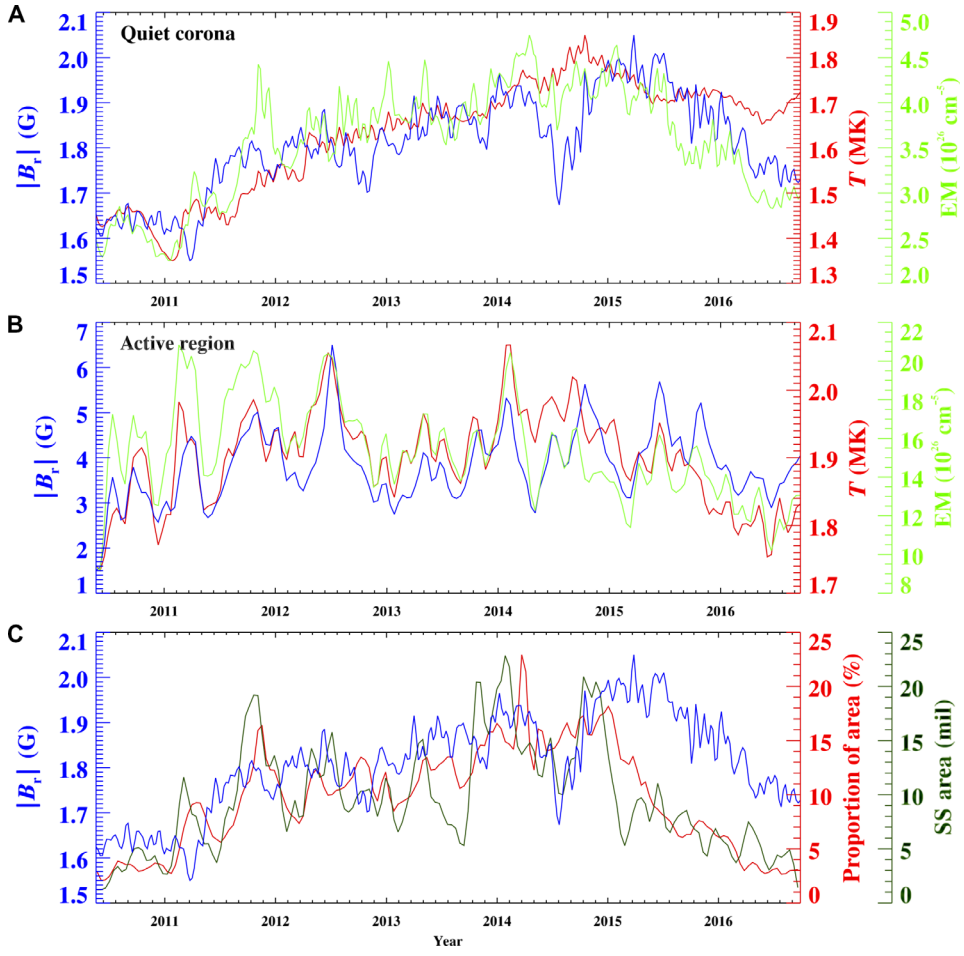

Fig. 3. Global means of various coronal and photospheric properties over the current solar cycle. Shown here are mean absolute magnetic field (blue), temperature (red), and EM (light green) for (**A**) quiet corona and (**B**) active regions. (**C**) Comparison of long-term changes in sunspot area (dark green), active region area (red), and quiet Sun magnetic field magnitude (blue). To reduce the dominant effect of the solar rotation and other short-term variation, all values have been smoothed in time with a Gaussian kernel of half-width 14 days. Daily sunspot area is sourced from http://solarscience.msfc.nasa.gov/greenwch.shtml.

The time series for active regions, and to a lesser extent the quiet corona, shown in Fig. 3 show interesting modulations with a quasi-annual periodicity. These modulations are likely a coronal response to the quasi-biannual periodicities of the solar dynamo found by helioseismology and other measures (*36*, *37*) and will be examined in detail in a future study. For active regions, the modulations seem to be driven by variations in high-temperature emission (see Fig. 4B), and this is related to the area of active regions—larger active regions tend to have more intense fields, higher EM, and increased emission at high temperature; thus, a quasi-periodicity in their size results in modulations in their global properties.

Figure 5 shows a subset of temperature and EM synoptic maps throughout the 7-year period. Inspection of the full set of synoptic maps aids the interpretation of the plots in Fig. 3 and supports an established model for the changing conditions in the quiet corona over the cycle. Regions of enhanced emission and temperature in the quiet corona extend in longitude from the sites of decayed active regions, stretched by differential rotation of the solar atmosphere (*38*) and corona (*39*) and following the distribution of enhanced photospheric fields. The quiet Sun magnetic field remains enhanced for a long period following active region decay, and the relative rate of decay and dissipation leads to a gradual increase over periods of years, as seen in Fig. 3A. That the temperature does not follow the same pattern shows the absence of a simple one-to-one relationship between photospheric magnetic field strength and coronal temperature, as shown previously for comparisons of hot plasma emission with magnetic field features (*40*). This may be explained by the connectivity of the lowest atmosphere to the overlying corona, which evolves with the solar cycle (*41*), and at least 50% of the photospheric flux closes in the low atmosphere (*42*). The configuration of the magnetic field in the isolated quiet corona compared to regions of decayed active regions may have an effect both on the transport of hot material from the chromosphere/transition region or on the efficiency of direct heating in the corona. For example, regions next to active regions often appear as dark, cool canopies (*43*). Referring to Fig. 3C, the peak in cross-correlation between active region area and quiet Sun field is 55% at a lag of 86 days. A quiet Sun field component, generated at small scales (*44*, *45*), is not likely to vary with the solar cycle (*46*)—the long-term quiet Sun variations we observe are consistent with the active region advection/fragmentation, and the lag compares well with estimates of decay time for small-scale magnetic elements in the quiet Sun (*47*).

A future study will investigate in more detail the changes in quiet Sun temperature distributions. In particular, we have not identified which regions are dominated by the 3-MK high-temperature peak shown in Fig. 4A, whether these are always associated with active region

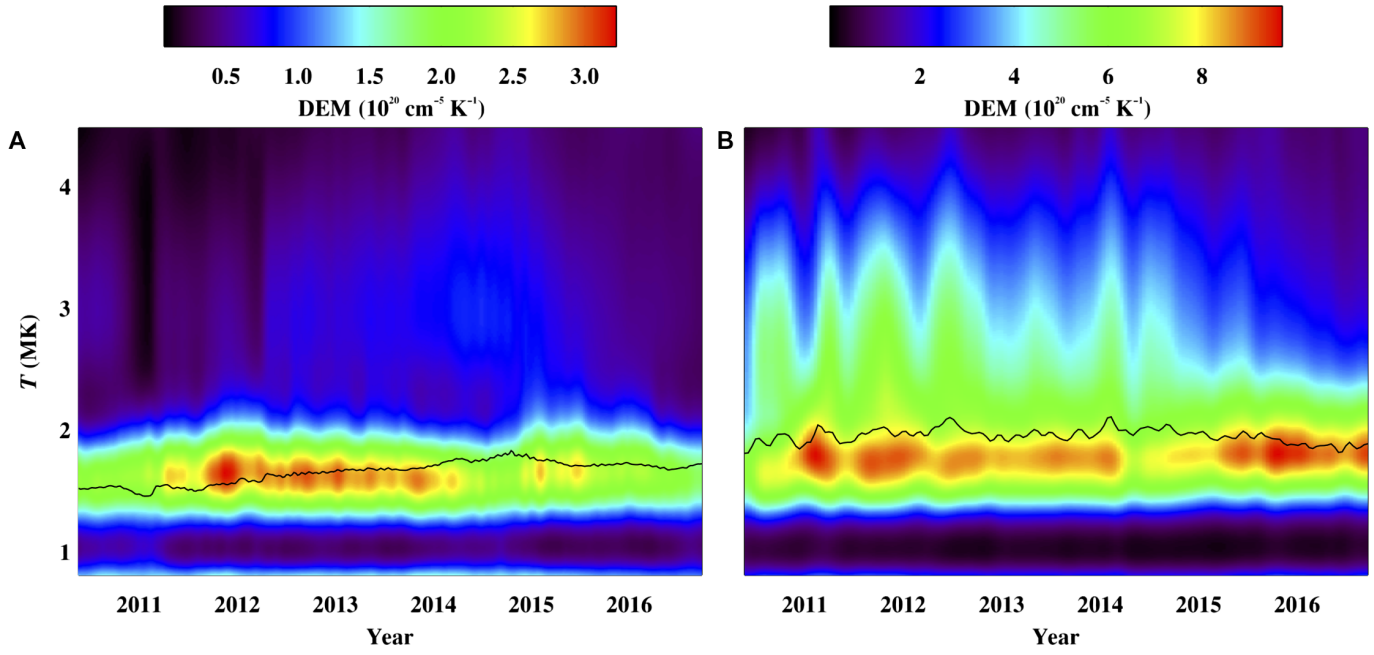

Fig. 4. The changing distribution of emission as a function of temperature over the current solar cycle. (**A**) Quiet corona and (**B**) active region DEM as a function of time over the current solar cycle. The *y* axis shows log temperature, with the DEM profiles strongly peaked at ~1.6 MK for the quiet corona and a broader peak at ~1.8 MK for active regions. The black curve shows the DEM-weighted mean temperature against time.

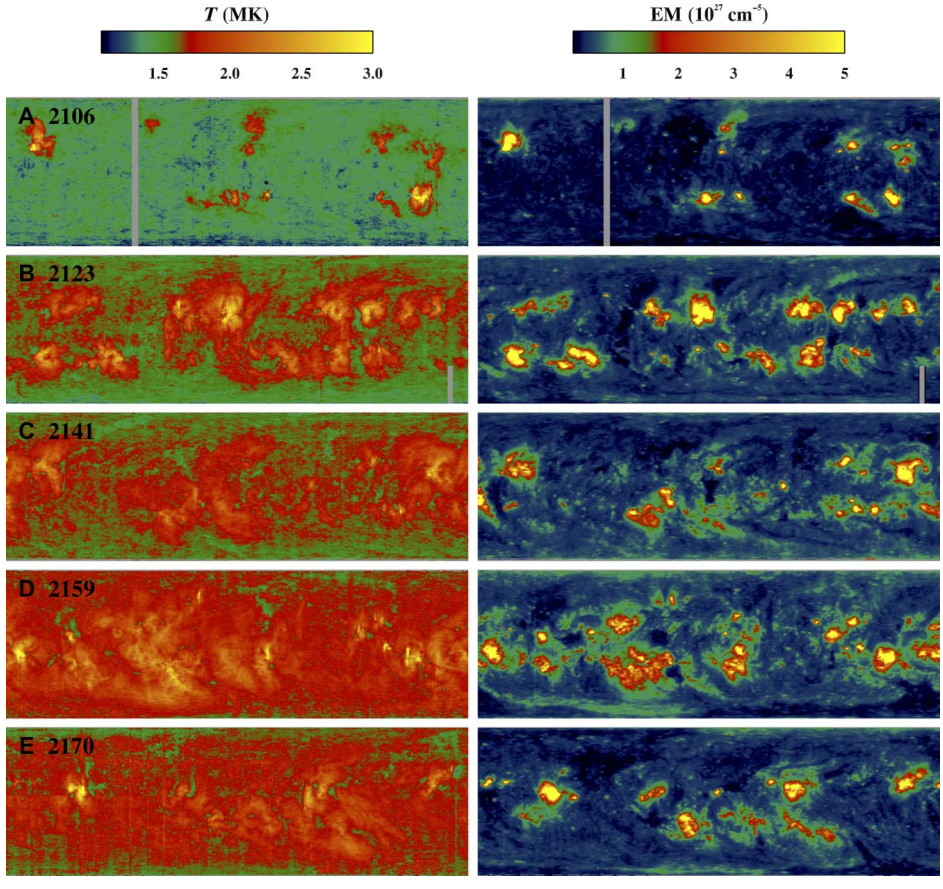

Fig. 5. The increasing global mean temperature and emission measure over the current solar cycle. Synoptic maps of mean temperature (left) and EM (right) for five solar rotations from 2010 to 2017. The Carrington rotation numbers are labeled in the plots, and each rotation is centered on dates 03 February 2011, 11 May 2012, 14 September 2013, 14 February 2015, and 11 December 2015.

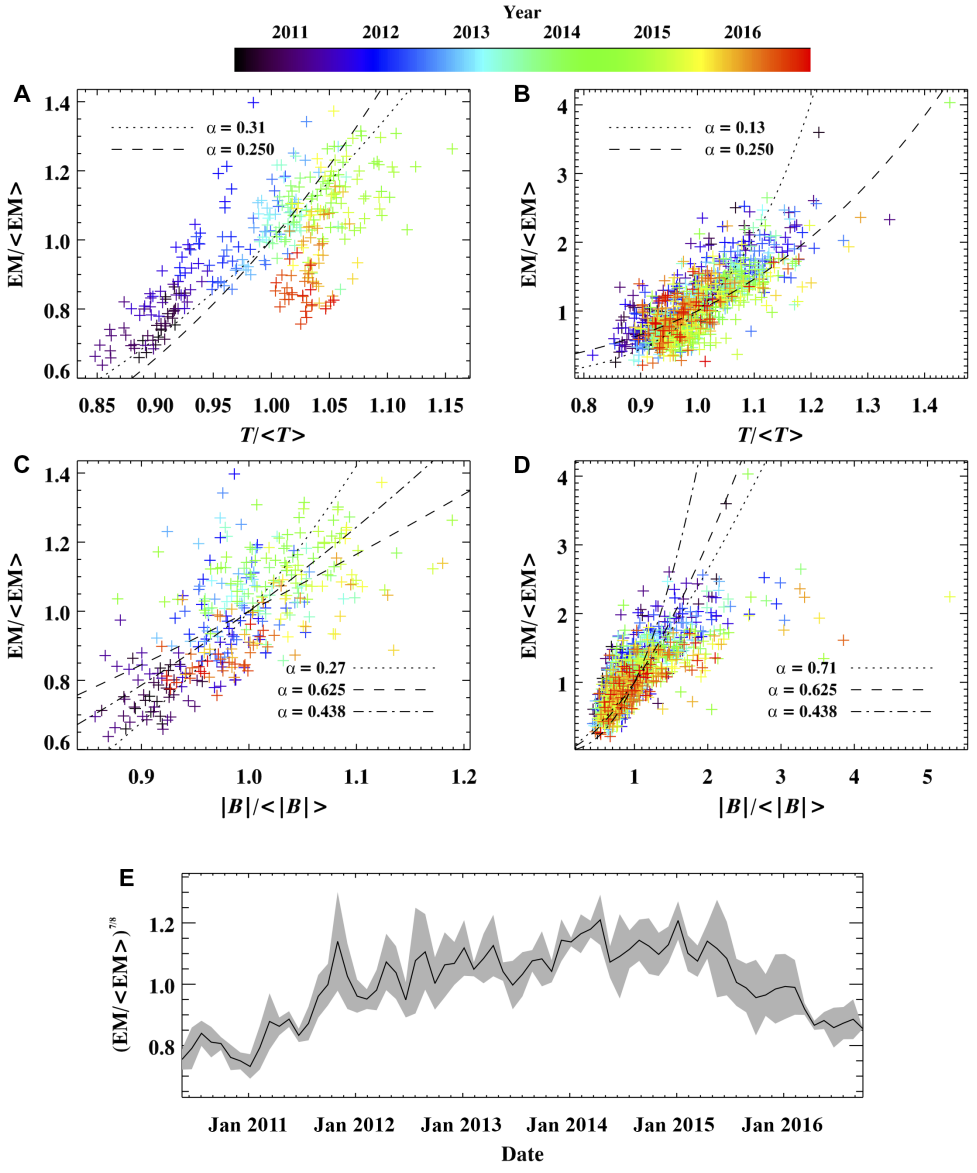

Fig. 6. Comparing various global properties of the corona and photosphere throughout the current solar cycle. EM against temperature for (**A**) quiet corona and (**B**) active regions and EM against magnetic field magnitude for (**C**) quiet and (**D**) active regions. For the quiet corona, each point represents the mean value over a 30° rotation, whereas for active regions, each point represents the mean value of each region. The dashed line in (A) and (B) shows the expected power law for hydrostatic loops (β = 0.25; see Methods), and the dotted line gives the best-fit power law. The dashed and dotted-dashed lines in (C) and (D) show theoretical curves for ac (α = 0.625) and dc (α = 0.438) heating mechanisms (see Methods), whereas the dotted line shows the best fit. The normalized values for quiet corona and active regions are achieved by dividing by the all-time means for quiet corona and for active regions, respectively. The color of the points represents time from 2010 to 2017, progressing through black, blue, green, yellow, and red, as shown in the color bar. (**E**) Variation of normalized quiet coronal EM raised to a power of 7/8 against time. The shaded area gives the SD of values in each time bin of a Carrington rotation (~1 month).

decay, and over what periods the high-temperature tails persist. The global, long-term means of EM and temperature (shown in Fig. 3A) must be influenced by the changing proportion of areas of different characteristics within the quiet Sun. In the context of modeling the ultraviolet solar irradiance, Fontenla *et al.* (*48*) show a detailed analysis of the relative area of several quiet Sun regions between 2010 and 2015 and segment the quiet Sun into several different categories such as plage, facula, and other subcategories. A similarly detailed region-by-region study of the quiet Sun should be made in the context of coronal temperature diagnostics and energy budget.

Figure 6A shows the relationship between quiet coronal EM and temperature. Fitting the distribution to a power law gives a 0.31 power of EM versus temperature (see Eq. 3 in Methods), compared to a predicted value of 0.25 for a representation of the quiet corona as a collection of hydrostatic loops [based on the scaling laws (*49*) and other simplifying assumptions]. At solar minimum (black points), temperature and EM are low. Points rise rapidly to the top right of the plot toward solar maximum in 2015. Red points, measured from 2015 to 2017, follow a rapid and consistent pattern of returning to solar minimum EM values, whereas temperature drops less rapidly; thus, the quiet corona has quite different global characteristics during the ascending and descending phases of the cycle. Active region EM and temperature (Fig. 5B) also show a consistent relationship. This relationship is surprising given the current understanding of active region warm

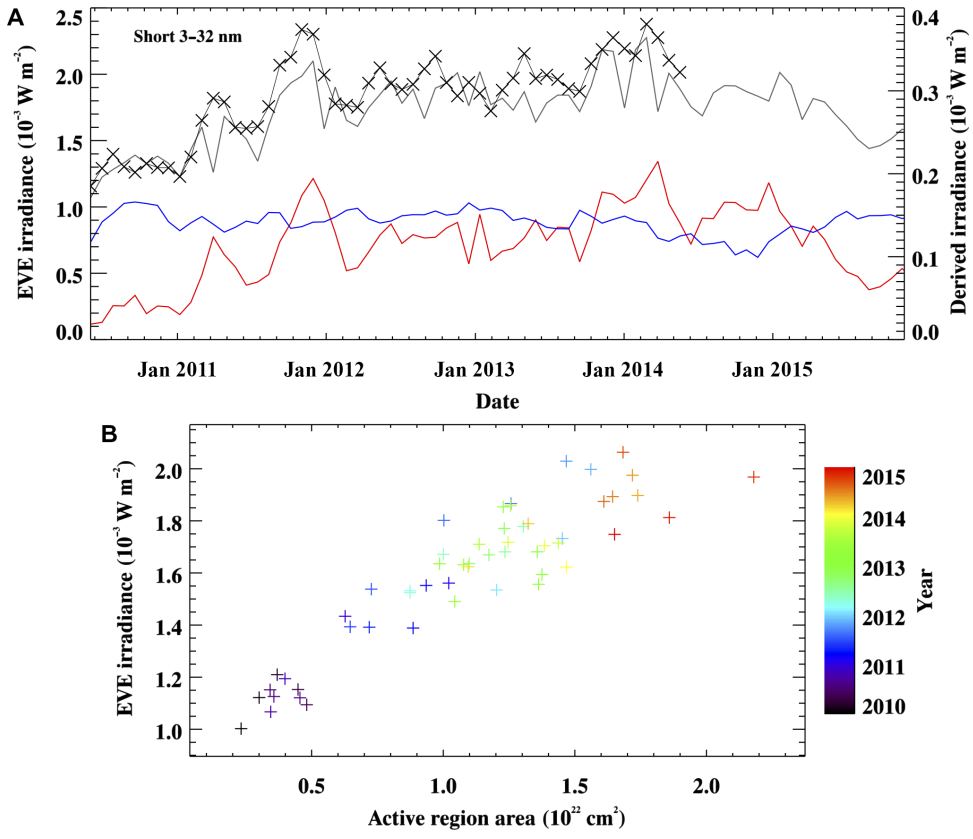

Fig. 7. Estimates of the EUV irradiance of the corona over the current solar cycle. (**A**) Estimated short-wavelength (3- to 32-nm) EUV irradiance at Earth orbit (thin black line) calculated from the DEM maps covering the whole visible disk (see Methods). Also shown are the active regions (red) and quiet coronal (blue) components calculated for the limited latitudinal range used in the rest of this study. These are compared to measurements by EVE (black) integrated over the short-wavelength (3- to 32-nm) band. The short-band EVE measurements unfortunately end in May 2014. (**B**) Measured EVE irradiance in the short spectral band as a function of active region area. The color of the points represent time from 2010 to the end of EVE short-band measurements in 2014, passing through black, blue, green, yellow, and red, as shown in the color bar.

loops, which are overdense compared to the hydrostatic prediction (*50*). These results, for the global corona over long time scales, show potential because they show consistency with the scaling laws.

The relationship between magnetic field and EM is shown in Fig. 5C for the quiet corona and shows some consistency. The distribution of active region values seen in Fig. 5D also shows a clear relationship. Similar relationships have been observed previously between, for example, an active region's photospheric magnetic field power spectrum and x-ray emission (*51*–*53*), and are important for models of active region heating. Active regions account for a large portion of the coronal energy budget, and the B-field/EM relationship must provide an important constraint on the nature of their heating. This is a study of global values averaged over large regions and long time periods. A more detailed approach is required where individual regions are tracked in time over hours (rather than taking a meridional sample), with a more thorough accounting of multithermality (rather than calculating a weighted mean temperature), an inversion of EM to estimate densities, and a more physical modeling of the coronal magnetic field. However, the clear relationships in global values shown in Fig. 6 are promising for a more advanced future study.

On the basis of the scaling laws and a hydrostatic assumption, variations in the average heating rate are expected to be proportional to variations in the EM, raised to a power of 7/8 (see Methods). This value is plotted for the quiet corona for years 2010 to 2017 in Fig. 5E. Heating rates are lowest during solar minimum, rising rapidly to 2012 and maintaining high values before declining from early 2015 to solar minimum values. As shown in Fig. 6E, the heating rate in the quiet corona may change by up to 50% in the rise from solar minimum—this variation cannot be solely attributed to variations in the magnetic field strength. The correlation between the EM and temperature of the quiet corona shown in Fig. 6A implies a correlation between the EM and the heating rate. On the other hand, the discrepancies and the large scatter of points in Fig. 6C for the quiet corona suggest that the strength of the magnetic field is not the only factor that determines the average heating rate. Motions transverse to the magnetic field due to Alfven waves or other disturbances may vary in amplitude with the solar cycle and significantly influence the heating rate.

On the basis of the DEM analysis, Fig. 7A shows estimated EUV irradiance in the short-wavelength regime, compared to EVE measurements. The derived EUV irradiance, using an empirical model based on our DEM estimates (see Methods), is around a factor of 4 lower than the measured irradiance. The primary reason for this is our limited temperature coverage so that potentially intense chromospheric or transition region lines are neglected. Inclusion of chromospheric temperature ranges gives a close agreement with irradiance observations, as shown in a recent study (*48*). Other reasons for the low modeled irradiance are given in Methods. What is striking is the close correlation between the measurements and the derived irradiance (~90% correlation). At these short wavelengths (3 to 32 nm), the short-term variability and general increase from solar minimum are dominated by the

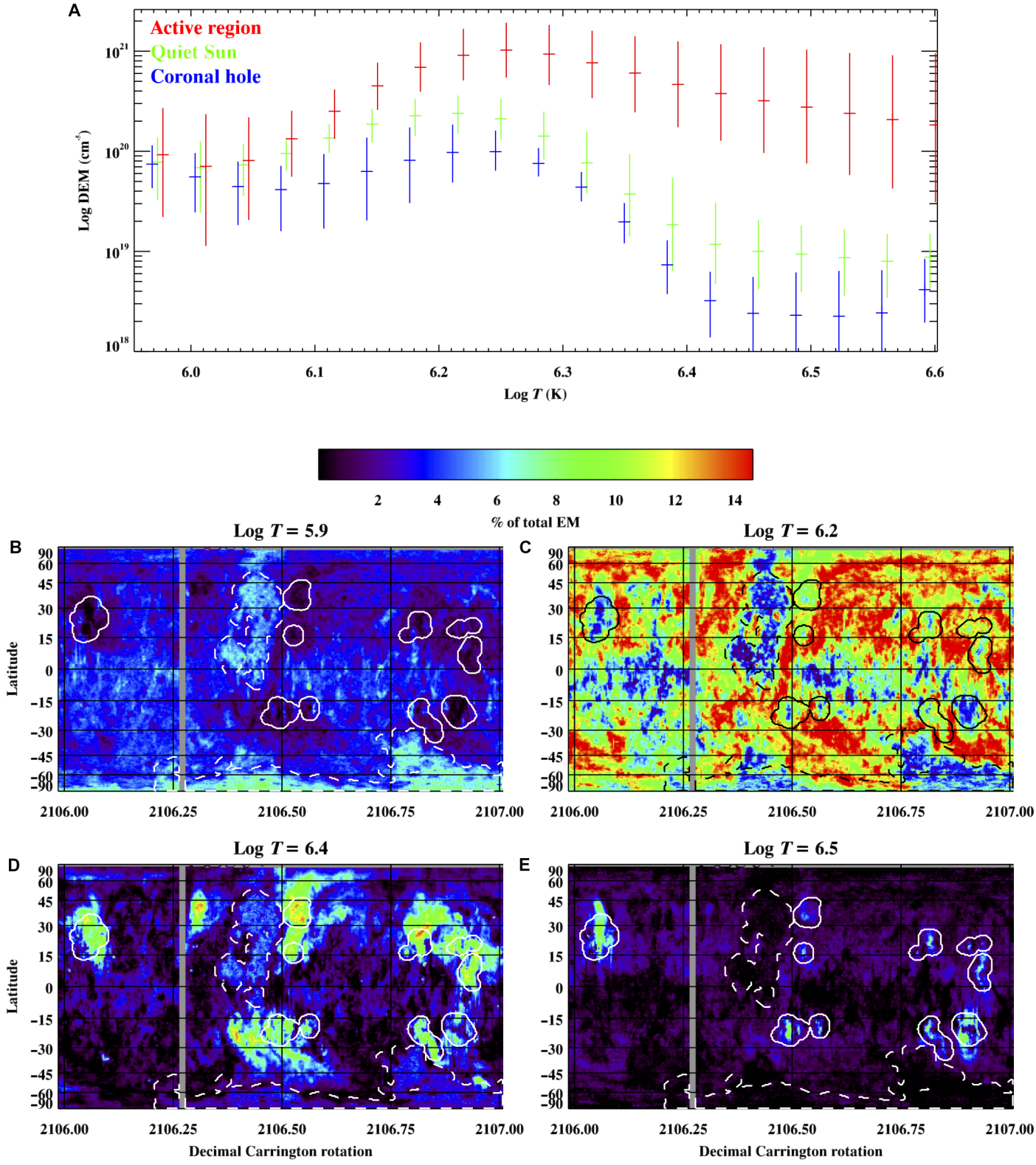

Fig. 8. Data from a whole Carrington rotation near solar minimum are used here to illustrate the DEM results. (**A**) DEM profiles averaged over the whole rotation for active regions (red) and quiet corona (green). The error bars show the SDs of DEM for each temperature bin. The quiet coronal DEM is strongly peaked near log $T = 6.2$. The active region DEM peaks near log $T = 6.25$ and decreases far more slowly with increasing temperature. (**B** to **E**) Maps of normalized DEM at four different temperatures, as indicated in the plot titles. The normalized DEM is the emission at that temperature as a percentage of the total emission at that pixel. Active regions are bounded by solid contours, whereas coronal holes are bounded by dashed contours.

increase in active region area (red line in Fig. 3C). The quiet coronal component is far smoother and remains fairly constant over the cycle. During 2010, the quiet coronal component is dominant as expected from the small number of active regions. Even during the period of solar maximum 2012–2017, the quiet coronal contribution is comparable to the active region component. The area-normalized quiet corona EUV irradiance is correlated with the solar activity (~40% increase from minimum to maximum), following the EM and temperature time series of Fig. 3A. The small dip in quiet coronal irradiance during 2014 to 2016 is thus caused by the decrease in quiet coronal area as active region area increases. The solar EUV irradiance therefore is composed of two main components—a quiet coronal component that changes smoothly and an active region component that varies rapidly due to the appearance and decay of active regions. The modeled irradiance shown in Fig. 7 is the irradiance component due to the hot, optically thin corona, gained directly from a hydrostatic model of the corona based on the AIA/SDO DEM profiles. To include the complete chromospheric and transition region irradiance, empirical estimates of the emission from different subcategories of areas within the quiet Sun and active regions must be included (*48*).

As the cycle evolves from minimum to maximum, the short-wavelength EVE irradiance increases rapidly in relation to the increase in the area of the solar disk covered by active regions, with an initial prominent peak in early 2012 (see Fig. 3C). Figure 7B shows the relationship between EVE irradiance and our estimate of active region area. There is an approximate linear relationship between measured irradiance and active region area, although other factors contribute to a large scatter, including variations in active region properties (density and temperature) and quiet coronal variations. In summary, the EUV irradiance received at Earth cannot be accurately estimated directly from simple indices of solar activity (for example, sunspot area). Although sunspot and active region area are the dominant factors that drive large variations on time scales of months or less, over the cycle, there are other factors such as the quiet coronal component and the long-term variations in active region EM and temperatures that must also be included.

DISCUSSION

Emerging flux, forming sunspots, is the dominant factor in driving the variation of the global corona, resulting in active region formation and evolution and, on active region decay, for example, (*54*), changes in the global quiet corona. New magnetic flux is input into the corona through the emergence of intense field in the form of looped flux ropes, appearing as sunspots on the photosphere and as active regions in the low corona. The active region field is transported gradually through photospheric motions and reconfigured through reconnections (*55*–*57*) and drives variations in the magnetic field of the quiet corona with a lag of a few weeks. The response of the quiet coronal EM is in high correlation with the magnetic field. The magnetic field remains enhanced for long periods in the quiet corona and over the cycle increases to peak in 2015: The quiet corona is therefore a store for the dissipated field of decayed active regions. Globally, we estimate a modest increase of less than 0.5 G in the mean magnitude of the quiet Sun field. The mean quiet coronal temperature sees a gradual increase of ~0.4 MK between the 2010 minimum and 2015 and a 50% rise in EM. The rise in quiet corona mean temperature is due to the increasing hot-component emission at ~3 MK, whereas the peak, or bulk, emission remains fairly constant at ~1.6 MK. Quiet coronal EM and high-temperature emission both decline in early 2015, with EM dropping rapidly close to solar minimum values. Mean temperature shows a more shallow decrease and has not yet reached minimum values. An intriguing result is that the main emission of both quiet corona and active regions is strongly peaked at ~1.6 and 1.8 MK, respectively, and remains markedly constant over the solar cycle. Long-term variations are due to variations in emission at high temperatures. For the quiet corona, this is a secondary peak in emission at ~3 MK that increases to a maximum in mid-2014, then consistently decreases to 2017. For active regions, there is an extension of the main broad DEM profile to higher temperatures that seems to modulate with a quasi-annual periodicity from 2010 to mid-2014, then decrease consistently to 2017. There must be an important mechanism or magnetic structural change that drives this modulation in high-temperature emission that is linked to the solar cycle.

The relationship between global coronal conditions and indices of solar activity such as active region area is complicated. We have not addressed the important issue of the cyclic dependence on latitude of emerging flux that must have an important influence on subsequent flux cancellation across the equator and rates of active region decay. Also important is the large-scale coronal magnetic field structure, its relation to the solar cycle (*41*), and coronal differential rotation (*39*). To make further connections and to further exploit current and future data sets, large-scale statistical studies must address two main issues: (i) the LOS EUV emission must be resolved through tomography (*28*, *58*, *59*), thus giving a three-dimensional (3D) map of conditions, and (ii) the coronal magnetic field must be estimated through model extrapolation of the observed photospheric field. The main challenges lie in the development of new improved methods and computational resources. Solving these challenges will allow constraint by a statistical study of local detail rather than by a global study. Such developments will give the diagnostics required to advance the field, giving ground truth to models and simulations, and the tools to fully exploit current and future high-resolution observations of the solar atmosphere.

METHODS

Calculation of EM and temperature

The emission of the main emitting ion in a given channel of the AIA/SDO is, to first order, proportional to the LOS integration of a function of density squared and the temperature distribution. The different response of each channel to temperature, calculated using theoretical and laboratory measurements of an optically thin plasma in equilibrium, allowed an estimate of the emission as a function of temperature—this is the widely used DEM approach. The CHIANTI atomic database (*60*) is used to calculate the theoretical contribution function, $G_{ji}(T,n_e)$, of line emission as a function of electron density n_e and temperature T, under an assumption of an optically thin plasma in equilibrium. This can give the line intensity given a density distribution along distance h of an LOS

$$I = \text{const} \times \int_{\text{LOS}} G_{ij}(T,n_e) n_e^2 dh \quad (1)$$

The response of the instrument channel as a function of wavelength and the contribution functions of all known emission lines within that channel were used to calculate the channel's temperature response $K(T)$. Defining the DEM as $\varphi(T) = n_e^2 \, dh/dT$ and using Eq. 1, the measured intensity is

$$I = \int K(T)\varphi(T)dT \quad (2)$$

Thus, the unknown density and temperature distribution along the LOS (Eq. 1) was reduced, through the assumption of an optically thin plasma to an unknown temperature distribution (Eq. 2). The inversion problem is to estimate the DEM given the observed intensities of several channels. Many different methods have been used to solve this ill-posed problem. Here, we used the fast and robust method of Hannah and Kontar (*27*), which relies on the Tikhonov regularization. Estimates of measurement errors are made by combining the estimated noise (by analyzing image areas that contain very little signal near the edge of the AIA field of view) with estimates of calibration uncertainties. Systematic errors may arise from calibration uncertainties. Here, we adapted the latest AIA calibration routines, which use cross-calibration with the EVE instrument (*61*). For each pixel, we calculated a DEM curve, similar to the profiles shown in Fig. 8A. EM is calculated by integrating the DEM. A single "temperature" is calculated through a DEM-weighted mean. One weakness in this approach is the multithermality of the plasma—there can be multiple peaks in the DEM and/or very broad peaks. Thus, the mean temperatures (for example in Fig. 3) should not generally be interpreted as the dominant temperature of the emitting plasma. Changes in the temperature, however, do give an indication of underlying changes in the DEM curves.

Figure 8 shows the DEM results as applied to a whole Carrington rotation near solar minimum. Figure 8A shows the mean DEM curves for quiet corona and active regions for this Carrington rotation. Quiet coronal DEMs are strongly peaked near 1.5 MK. For these, a weighted mean temperature is a meaningful value—it is a reasonable representation of the most probable temperature of the emitting plasma. For active regions, the DEM profiles have very broad peaks above ~1.8 MK. For the sake of presentation, it was interpreted in this study as a temperature, although it is not truly representative of the bulk of the emitting plasma. A more detailed analysis of these results, possibly incorporating multithermality through the fitting of the DEM profiles to analytical functions, will be made in a future study. Figure 8 (B to E) shows how active regions and quiet corona have considerable differences in the temperature dependency of their emission. To visualize this, the DEM for each point in the map was divided by the total integrated DEM at that point. These maps show, therefore, the fraction of the total emission at that temperature. Figure 8B shows a low temperature of ~0.8 MK, where the strongest fraction of emission is from the coronal holes. Conversely, active regions are dark, showing that only a very low fraction of their total emission is at a low temperature. At $T \approx 1.5$ MK (Fig. 8C), the quiet corona is emitting most strongly. Broad regions of the quiet corona are depicted in red, indicating that around 15% of the plasma is emitting at this temperature range. Above this temperature, active regions dominate, as shown in Fig. 8 (D and E). At $T \approx 3$ MK (Fig. 8E), only the cores of active regions have any strong emission. Coronal holes are not considered in our main results. Their DEM profiles may peak at temperatures close to, or below, the considered temperature range—that is, DEMs obtained using the AIA/SDO iron-dominated channels are not best suited for cooler regions. Furthermore, the segmentation method does not distinguish between filament channels and coronal holes—for this, additional magnetic field data are required (*62*).

Magnetic field measurements

HMI/SDO makes measurements of the LOS photospheric magnetic field (B_{LOS}) through Zeeman splitting of an emission line. The radial magnetic field component B_r is derived from B_{LOS} using a simple geometrical correction. Here, we used the high-resolution B_r synoptic maps provided by the instrument team. The synoptic maps are smoothed with a sliding window median, from which the absolute value is further smoothed by convolution with a Gaussian kernel. The first smoothing stage removes much of the small-scale photospheric variation and helps to isolate the excess flux arising from a given region. The second smoothing of the magnetic field magnitude enables a far cleaner region-by-region comparison with the AIA data and is necessary for identifying different coronal regions.

Creation of synoptic maps and global mean values

The DEM profiles, calculated for each observed pixel, were used to create the final synoptic maps. A strip of DEM profiles, taken within a few degrees of the Sun disk's central meridian, was extracted. These were stacked in time, and as the Sun rotates over ~27 days from Earth's perspective, a synoptic data cube of DEM profiles over a whole rotation was built [with dimensions longitude (or time), latitude, and temperature]. The data cubes were rebinned into regular longitude and latitude and were stored as one data cube for each solar (Carrington) rotation over the 2010–2017 period. Because the data from six AIA channels, with a selected ~1-hour time step, were used to create a single data cube, the whole unreduced data set contained ~250,000 images, reduced to a set of over 90 data cubes. From these, we gained the mean temperature and total EM, which, with the HMI magnetic field maps, provided the reduced data for the remainder of the analysis. An example of these final synoptic maps is shown in Fig. 2. Areas in the maps with predominant temperature $T > 1.82$ MK, EM $> 1.6 \times 10^{27}$ cm^{-5}, and $|B_r| > 7$ G are defined as active regions and are shown within white/black contours. Cooler, low-mass regions are coronal holes, often found at the poles. These are identified as regions with predominant temperature $T < 1.39$ MK and EM $< 1.7 \times 10^{26}$ cm^{-5} and are excluded from the study. Areas that are not coronal holes and have $T < 1.82$ MK, EM $< 1.6 \times 10^{27}$ cm^{-5}, and $|B_r| < 7$ G are defined as quiet corona, shown as areas outside the dotted contours in Fig. 2. There are narrow boundaries between defined regions that are excluded from the study, being regions that do not satisfy the above thresholds in all three parameters. For a study of quiet corona temporal variation, a mean value is calculated over longitudinal bins of 30°, giving 12 values for each full rotation; roughly a thousand values over the whole time period. For active regions, each region was treated as a single area from which the mean properties were calculated. Occasionally, it is difficult to distinguish between two neighboring active regions, in which case the regions were combined to calculate a single set of mean values.

Power law relationships between global coronal values

By representing the quiet corona as a collection of hydrostatic loops, we may establish relationships between their temperature, density, and heating rate. The Rosner-Tucker-Vaiana (RTV) scaling laws, originally proposed for uniformly heated loops (*63*), were extended to include a wider class of hydrostatic loops (*49*). The isobaric approximation can be adopted for loops whose summits are much below a coronal scale height of a few tens of megameters. For structures with a typical temperature of 1 MK, the pressure scale height is about 50 Mm. On the other hand, a 15-Mm-long semicircular loop will have a summit height of around 5 Mm. The emission from the upper layers of the atmosphere is expected to be low as density drops with height. In the lower parts of the atmosphere, the emission is dominated by the more common short loops that can be treated as isobaric. However, Fig. 1 shows bright long loops concentrated around active regions that may contribute to the discrepancy seen in Fig. 6 for active regions. Therefore, a more detailed future study of a particular region will require the inclusion of a finite scale height that

would lead to more accurate relationships between temperature and EM. The scaling laws for near-isothermal and isobaric loops read

$$T \sim (\rho L)^{1/2} \exp\left(-0.12\frac{L}{s_H}\right) \quad (3)$$

$$H_0 \sim T^{7/2} L^{-2} \exp\left(0.78\frac{L}{s_H}\right) \quad (4)$$

where T, ρ, L are the temperature, density, and loop length, respectively. The coronal base heating rate at some height $s = s_0$ is denoted by H_0, and the heating scale length is denoted by s_H. Uniform heating corresponds to $s_H = \infty$. Assuming that the loop length L and the heating scale length s_H do not change in time, we derive the following relationship from Eq. 3

$$\frac{T(t)}{T(0)} = \left(\frac{\rho(t)}{\rho(0)}\right)^{1/2} \cong \left(\frac{EM(t)}{EM(0)}\right)^{1/4} \quad (5)$$

where t denotes time and EM denotes EM. For Fig. 6A, rather than use values at $t = 0$ in the denominator, we used the all-time mean value of quiet corona EM, $\langle EM \rangle$, and the all-time mean of quiet corona temperature, $\langle T \rangle$. Similarly for Fig. 6B, the all-time means for active regions was used. The dashed line in Fig. 6A shows the expected value for a hydrostatic atmosphere as given by Eq. 5. Variations in the heating rate of the base are determined by

$$\frac{H_0(t)}{\langle H_0 \rangle} = \left(\frac{\rho(t)}{\langle \rho \rangle}\right)^{7/4} \cong \left(\frac{EM(t)}{\langle EM \rangle}\right)^{7/8} \quad (6)$$

where a uniform coronal base $s = s_0$ is assumed. This is the basis for Fig. 6E. Note that the derived relationships do not depend on loop length and can be applied to loops with different lengths.

Figure 6 (C and D) investigates the relationship between magnetic field B and EM. The likelihood of wave (ac) versus stress (dc) heating has previously been investigated for active regions by setting a uniform heating rate in proportion to the heat flux at a loop base and assuming a time-constant average transverse velocity (*1*). The following relationship between magnetic field and EM (~density) is established

$$\frac{B(t)}{B(0)} = \left(\frac{\rho(t)}{\rho(0)}\right)^{2\alpha} \cong \left(\frac{EM(t)}{EM(0)}\right)^{\alpha} \quad (7)$$

where $\alpha = 5/8$ for an ac and $\alpha = 7/16$ for a dc heating mechanism. These are plotted as dashed and dotted-dashed curves in Fig. 6 (C and D). Similar to Eq. 5 (EM versus T), the data points were divided by their all-time quiet corona and active region means, respectively.

The dotted line in Fig. 6 (A and B) is a minimization of the function

$$\sum_i \left| \frac{T_i(t)}{(\langle T \rangle + c)} - \left(\frac{EM_i(t)}{\langle EM \rangle}\right)^{\beta} \right| \quad (8)$$

with respect to parameters β and c. c is a small correction factor that allows for a systematic calibration error (found to be <2% of the mean value for both quiet corona and active regions). Similarly, the dotted line in Fig. 6 (C and D) is a minimization of the function

$$\sum_i \left| \frac{B_i(t)}{(\langle B \rangle + c)} - \left(\frac{EM_i(t)}{\langle EM \rangle}\right)^{\alpha} \right| \quad (9)$$

with respect to α and d. As in Eq. 8, d is a small correction factor found to be <2% of the mean value for both quiet corona and active regions.

Measurement and model estimate of EUV irradiance at Earth orbit

EVE/SDO makes measurements of the solar irradiance emitted by the whole corona in high spectral resolution and is used here as a comparison for modeled coronal EUV irradiance over the solar cycle. The EUV intensity is integrated over the whole corona, so EVE cannot directly distinguish between emissions from different regions. To calculate the coronal irradiance, we (i) estimated density by inverting the EM within each temperature bin of the DEM maps along LOSs with scale heights set by the temperature assuming hydrostatic equilibrium, (ii) used the temperature, density, and the Chianti atomic database (*60*) to calculate the line emission and continuum along each LOS, and (iii) integrated the emission along each LOS and over all temperature bins. The irradiance was calculated for all pixels within the synoptic maps, giving the total derived irradiance shown in Fig. 7A. The active regions and quiet coronal areas identified within a limited latitudinal range (within ±70° of the equator, wider than that used in the rest of this study) were also used to give an approximation of the irradiance from both active regions and quiet corona separately. The absolute values of derived irradiance are considerably lower than those measured. This is mainly due to the following: (i) the model does not include contributions from emission lines formed outside the DEM temperature range $0.8 < T < 6.5$ MK (for example, we have excluded the very strong He II 30.4-nm line because it is formed in the chromosphere and outside of the temperature range of our derived irradiance); (ii) the model does not include flares or other short-term variations; (iii) the model does not include off-limb regions; and (iv) for the case of the active region and quiet coronal components, the model is based only on a limited latitudinal range (that is, does not include areas above 70° from the equator).

REFERENCES AND NOTES

1. G. H. Fisher, D. W. Longcope, T. R. Metcalf, A. A. Pevtsov, Coronal heating in active regions as a function of global magnetic variables. *Astrophys. J.* **508**, 885–898 (1998).
2. S. R. Habbal, M. Druckmüller, H. Morgan, I. Scholl, V. Rušin, A. Daw, J. Johnson, M. Arndt, Total solar eclipse observations of hot prominence shrouds. *Astrophys. J.* **719**, 1362–1369 (2010).
3. H. Morgan, L. Jeska, D. Leonard, The expansion of active regions into the extended solar corona. *Astrophys. J.* **206**, 19 (2013).
4. G. Del Zanna, The multi-thermal emission in solar active regions. *Astron. Astrophys.* **558**, A73 (2013).
5. M. Hahn, E. Landi, D. W. Savin, Differential emission measure analysis of a polar coronal hole during the solar minimum in 2007. *Astroph. J.* **736**, 101 (2011).
6. C. David, A. H. Gabriel, F. Bely-Dubau, A. Fludra, P. Lemaire, K. Wilhelm, Measurement of the electron temperature gradient in a solar coronal hole. *Astron. Astrophys.* **336**, L90–L94 (1998).

7. S. R. Habbal, M. Druckmüller, H. Morgan, A. Daw, J. Johnson, A. Ding, M. Arndt, R. Esser, V. Rušin, I. Scholl, Mapping the distribution of electron temperature and Fe charge states in the corona with total solar eclipse observations. *Astrophys. J.* **708**, 1650 (2009).
8. S. R. Habbal, H. Morgan, M. Druckmüller, A. Ding, On the constancy of the electron temperature in the expanding corona throughout solar cycle 23. *Astrophys. J. Lett.* **711**, L75 (2010).
9. Š. Mackovjak, E. Dzifčáková, J. Dudík, Differential emission measure analysis of active region cores and quiet Sun for the non-Maxwellian κ-distributions. *Astron. Astrophys.* **564**, A130 (2014).
10. M. Hahn, D. W. Savin, Evidence for wave heating of the quiet-sun corona. *Astrophys. J.* **795**, 111 (2014).
11. J. A. Ionson, Resonant absorption of Alfvenic surface waves and the heating of solar coronal loops. *Astrophys. J.* **226**, 650–673 (1978).
12. A. J. C. Beliën, P. C. H. Martens, R. Keppens, Coronal heating by resonant absorption: The effects of chromospheric coupling. *Astrophys. J.* **526**, 478–493 (1999).
13. P. Antolin, K. Shibata, T. Kudoh, D. Shiota, D. Brooks, Predicting observational signatures of coronal heating by Alfvén waves and nanoflares. *Astrophys. J.* **688**, 669–682 (2008).
14. A. A. van Ballegooijen, M. Asgari-Targhi, S. R. Cranmer, E. E. DeLuca, Heating of the solar chromosphere and corona by Alfvén wave turbulence. *Astrophys. J.* **736**, 3 (2011).
15. E. N. Parker, Nanoflares and the solar X-ray corona. *Astrophys. J.* **330**, 474–479 (1988).
16. P. J. Cargill, The fine structure of a nanoflare-heated corona. *Sol. Phys.* **147**, 263–268 (1993).
17. G. Vekstein, Probing nanoflares with observed fluctuations of the coronal EUV emission. *Astron. Astrophys.* **499**, L5–L8 (2009).
18. B. De Pontieu, L. R. van der Voort, S. W. McIntosh, T. M. D. Pereira, M. Carlsson, V. Hansteen, H. Skogsrud, J. Lemen, A. Title, P. Boerner, N. Hurlburt, T. D. Tarbell, J. P. Wuelser, E. E. De Luca, L. Golub, S. McKillop, K. Reeves, S. Saar, P. Testa, H. Tian, C. Kankelborg, S. Jaeggli, L. Kleint, J. Martinez-Sykora, On the prevalence of small-scale twist in the solar chromosphere and transition region. *Science* **346**, 1255732 (2014).
19. M. J. Aschwanden, A. Winebarger, D. Tsiklauri, H. Peter, The coronal heating paradox. *Astrophys. J.* **659**, 1673–1681 (2007).
20. J. A. Klimchuk, S. J. Bradshaw, Are chromospheric nanoflares a primary source of coronal plasma? *Astrophys. J.* **791**, 60 (2014).
21. I. Ermolli, K. Matthes, T. Dudok de Wit, N. A. Krivova, K. Tourpali, M. Weber, Y. C. Unruh, L. Gray, U. Langematz, P. Pilewskie, E. Rozanov, W. Schmutz, A. Shapiro, S. K. Solanki, T. N. Woods, Recent variability of the solar spectral irradiance and its impact on climate modelling. *Atmos. Chem. Phys.* **13**, 3945–3977 (2013).
22. T. Woollings, M. Lockwood, G. Masato, C. Bell, L. Gray, Enhanced signature of solar variability in Eurasian winter climate. *Geophys. Res. Lett.* **37**, L20805 (2010).
23. M. Lockwood, Solar influence on global and regional climates. *Surv. Geophys.* **33**, 503–534 (2012).
24. J. R. Lemen, A. M. Title, D. J. Akin, P. F. Boerner, C. Chou, J. F. Drake, D. W. Duncan, C. G. Edwards, F. M. Friedlaender, G. F. Heyman, N. E. Hurlburt, N. L. Katz, G. D. Kushner, M. Levay, R. W. Lindgren, D. P. Mathur, E. L. McFeaters, S. Mitchell, R. A. Rehse, C. J. Schrijver, L. A. Springer, R. A. Stern, T. D. Tarbell, J.-P. Wuelser, C. J. Wolfson, C. Yanari, J. A. Bookbinder, P. N. Cheimets, D. Caldwell, E. E. Deluca, R. Gates, L. Golub, S. Park, W. A. Podgorski, R. I. Bush, P. H. Scherrer, M. A. Gummin, P. Smith, G. Auker, P. Jerram, P. Pool, R. Soufli, D. L. Windt, S. Beardsley, M. Clapp, J. Lang, N. Waltham, The *Atmospheric Imaging Assembly* (AIA) on the *Solar Dynamics Observatory* (SDO). *Sol. Phys.* **275**, 17–40 (2012).
25. P. H. Scherrer, J. Schou, R. I. Bush, A. G. Kosovichev, R. S. Bogart, J. T. Hoeksema, Y. Liu, T. L. Duvall Jr., J. Zhao, A. M. Title, C. J. Schrijver, T. D. Tarbell, S. Tomczyk, The *Helioseismic and Magnetic Imager* (HMI) Investigation for the *Solar Dynamics Observatory* (SDO). *Sol. Phys.* **275**, 207–227 (2012).
26. T. N. Woods, F. G. Eparvier, R. Hock, A. R. Jones, D. Woodraska, D. Judge, L. Didkovsky, J. Lean, J. Mariska, H. Warren, D. McMullin, P. Chamberlin, G. Berthiaume, S. Bailey, T. Fuller-Rowell, J. Sojka, W. K. Tobiska, R. Viereck, *Extreme Ultraviolet Variability Experiment* (EVE) on the *Solar Dynamics Observatory* (SDO): Overview of science objectives, instrument design, data products, and model developments. *Sol. Phys.* **275**, 115–143 (2012).
27. I. G. Hannah, E. P. Kontar, Differential emission measures from the regularized inversion of Hinode and SDO data. *Astron. Astrophys.* **539**, A146 (2012).
28. F. A. Nuevo, A. M. Vásquez, E. Landi, R. Frazin, Multimodal differential emission measure in the solar corona. *Astrophys. J.* **811**, 128 (2015).
29. L. Pradeep Chitta, R. Kariyappa, A. A. Van Ballegooijen, E. E. DeLuca, S. S. Hasan, A. Hanslmeier, Observations and modeling of the emerging extreme-ultraviolet loops in the quiet sun as seen with the solar dynamics observatory. *Astrophys. J.* **768**, 32 (2013).
30. D. H. Brooks, H. P. Warren, D. R. Williams, T. Watanabe, Hinode/extreme-ultraviolet imaging spectrometer observations of the temperature structure of the quiet corona. *Astrophys. J.* **705**, 1522–1532 (2009).
31. M. J. Aschwanden, P. Boerner, C. J. Schrijver, A. Malanushenko, Automated temperature and emission measure analysis of coronal loops and active regions observed with the *Atmospheric Imaging Assembly* on the *Solar Dynamics Observatory* (SDO/AIA). *Sol. Phys.* **283**, 5–30 (2013).
32. J. T. Schmelz, S. Pathak, D. H. Brooks, G. M. Christian, R. S. Dhaliwal, Hot topic, warm loops, cooling plasma? Multithermal analysis of active region loops. *Astrophys. J.* **795**, 171 (2014).
33. Y.-M. Wang, J. L. Lean, N. R. Sheeley Jr., Modeling the sun's magnetic field and irradiance since 1713. *Astrophys. J.* **625**, 522–538 (2005).
34. D. H. Hathaway, The solar cycle. *Living Rev. Sol. Phys.* **7**, 1 (2010).
35. F. Tang, R. Howard, J. M. Adkins, A statistical study of active regions 1967-1981. *Sol. Phys.* **91**, 75–86 (1984).
36. S. T. Fletcher, A.-M. Broomhall, D. Salabert, S. Basu, W. J. Chaplin, Y. Elsworth, R. A. Garcia, R. New, A seismic signature of a second dynamo?. *Astrophys. J. Lett.* **718**, L19–L22 (2010).
37. P. Beaudoin, C. Simard, J.-F. Cossette, P. Charbonneau, Double dynamo signatures in a global MHD simulation and mean-field dynamos. *Astrophys. J.* **826**, 138 (2016).
38. J. G. Beck, A comparison of differential rotation measurements—(Invited Review). *Sol. Phys.* **191**, 47–70 (2000).
39. H. Morgan, The rotation of the white light solar corona at height 4 $R_{\odot}$ from 1996 to 2010: A tomographical study of large angle and spectrometric coronagraph C2 observations. *Astrophys. J.* **738**, 189 (2011).
40. O. G. Badalyan, N. G. Bludova, Relation of the green coronal line intensity to sunspot areas and magnetic fields of different scales. *Sol. Syst. Res.* **48**, 305–315 (2014).
41. H. Morgan, S. R. Habbal, Observational aspects of the three-dimensional coronal structure over a solar activity cycle. *Astrophys. J.* **710**, 1–15 (2010).
42. R. M. Close, C. E. Parnell, D. H. Mackay, E. R. Priest, Statistical flux tube properties of 3D magnetic carpet fields. *Sol. Phys.* **212**, 251–275 (2003).
43. Y.-M. Wang, E. Robbrecht, K. Muglach, The evolution of dark canopies around active regions. *Astrophys. J.* **733**, 20 (2011).
44. J. Wang, H. Wang, F. Tang, J. W. Lee, H. Zirin, Flux distribution of solar intranetwork magnetic fields. *Sol. Phys.* **160**, 277–288 (1995).
45. C. Jin, J. Wang, Solar cycle variation of the inter-network magnetic field. *Astrophys. J.* **806**, 174 (2015).
46. D. Buehler, A. Lagg, S. K. Solanki, Quiet Sun magnetic fields observed by Hinode: Support for a local dynamo. *Astron. Astrophys.* **555**, A33 (2013).
47. A. D. Crouch, P. Charbonneau, G. Beaubien, D. Paquin-Ricard, A model for the total solar irradiance based on active region decay. *Astrophys. J.* **677**, 723–741 (2008).
48. J. M. Fontenla, M. Codrescu, M. Fedrizzi, T. Fuller-Rowell, F. Hill, E. Landi, T. Woods, Five years of synthesis of solar spectral irradiance from SDID/SISA and SDO/AIA images. *Astrophys. J.* **834**, 54 (2017).
49. S. Serio, G. Peres, G. S. Vaiana, L. Golub, R. Rosner, Closed coronal structures. II. Generalized hydrostatic model. *Astrophys. J.* **243**, 288–300 (1981).
50. A. R. Winebarger, H. P. Warren, J. T. Mariska, *Transition region and coronal explorer* and soft X-ray telescope active region loop observations: Comparisons with static solutions of the hydrodynamic equations. *Astrophys. J.* **587**, 439–449 (2003).
51. V. I. Abramenko, A. A. Pevtsov, P. Romano, Coronal heating and photospheric turbulence parameters: Observational aspects. *Astrophys. J. Lett.* **646**, L81–L84 (2006).
52. L. van Driel-Gesztelyi, P. Démoulin, C. H. Mandrini, L. Harra, J. A. Klimchuk, The long-term evolution of AR 7978: The scalings of the coronal plasma parameters with the mean photospheric magnetic field. *Astrophys. J.* **586**, 579–591 (2003).
53. P. Démoulin, L. van Driel-Gesztelyi, C. H. Mandrini, J. A. Klimchuk, L. Harra, The long-term evolution of AR 7978: Testing coronal heating models. *Astrophys. J.* **586**, 592–605 (2003).
54. N. Deng, D. P. Choudhary, A. Tritschler, C. Denker, C. Denker, C. Liu, H. Wang, Flow field evolution of a decaying sunspot. *Astrophys. J.* **671**, 1013–1021 (2007).
55. Y.-M. Wang, N. R. Sheeley Jr., Magnetic flux transport and the sun's dipole moment: New twists to the Babcock-Leighton model. *Astrophys. J.* **375**, 761–770 (1991).
56. V. I. Abramenko, L. A. Fisk, V. B. Yurchyshyn, The rate of emergence of magnetic dipoles in coronal holes and adjacent quiet-sun regions. *Astrophys. J.* **641**, L65–L68 (2006).
57. L. van Driel-Gesztelyi, L. M. Green, Evolution of active regions. *Living Rev. Sol. Phys.* **12**, 1 (2015).
58. R. A. Frazin, M. Jacob, W. B. Manchester IV, H. Morgan, M. B. Wakin, Toward reconstruction of coronal mass ejection density from only three points of view. *Astrophys. J.* **695**, 636–641 (2009).
59. H. Morgan, An atlas of coronal electron density at 5$R_{\odot}$. I. Data processing and calibration. *Astrophys. J. Suppl. Ser.* **219**, 23 (2015).
60. G. DelZanna, K. P. Dere, P. R. Young, E. Landi, H. E. Mason, CHIANTI—An atomic database for emission lines. Version 8. *Astron. Astrophys.* **582**, A56 (2015).
61. P. F. Boerner, P. Testa, H. Warren, M. A. Weber, C. J. Schrijver, Photometric and thermal cross-calibration of solar EUV instruments. *Sol. Phys.* **289**, 2377–2397 (2014).
62. C. Lowder, J. Qiu, R. Leamon, Coronal holes and open magnetic flux over cycles 23 and 24. *Sol. Phys.* **292**, 18 (2017).
63. R. Rosner, W. H. Tucker, G. S. Vaiana, Dynamics of the quiescent solar corona. *Astrophys. J.* **220**, 643–645 (1978).

64. H. Morgan, M. Druckmüller, Multi-scale Gaussian normalization for solar image processing, in *Coronal Magnetometry*, S. Tomczyk, J. Zhang, T. Bastian (Springer, 2014), pp. 323–333.

Acknowledgments: We acknowledge the software DEM inversion routines provided through www.astro.gla.ac.uk/~iain/demreg/. **Funding:** This work was possible due to a Research Fellowship from the Leverhulme Foundation to H.M. **Author contributions:** H.M. and Y.T. contributed equally to this work. **Competing interests:** The authors declare that they have no competing interests. **Data and materials availability:** All data needed to evaluate the conclusions in the paper are present in the paper. Additional data related to this paper may be requested from the authors. The data used in this work are courtesy of NASA/SDO and the AIA, EVE, and HMI science teams.

Submitted 29 August 2016
Accepted 13 June 2017
Published 14 July 2017
10.1126/sciadv.1602056

Citation: H. Morgan, Y. Taroyan, Global conditions in the solar corona from 2010 to 2017. *Sci. Adv.* **3**, e1602056 (2017).

Global conditions in the solar corona from 2010 to 2017

Huw Morgan and Youra Taroyan

Sci Adv **3** (7), e1602056.
DOI: 10.1126/sciadv.1602056